Soft Matter

www.rsc.org/softmatter

Volume 9 | Number 37 | 7 October 2013 | Pages 8775–9028

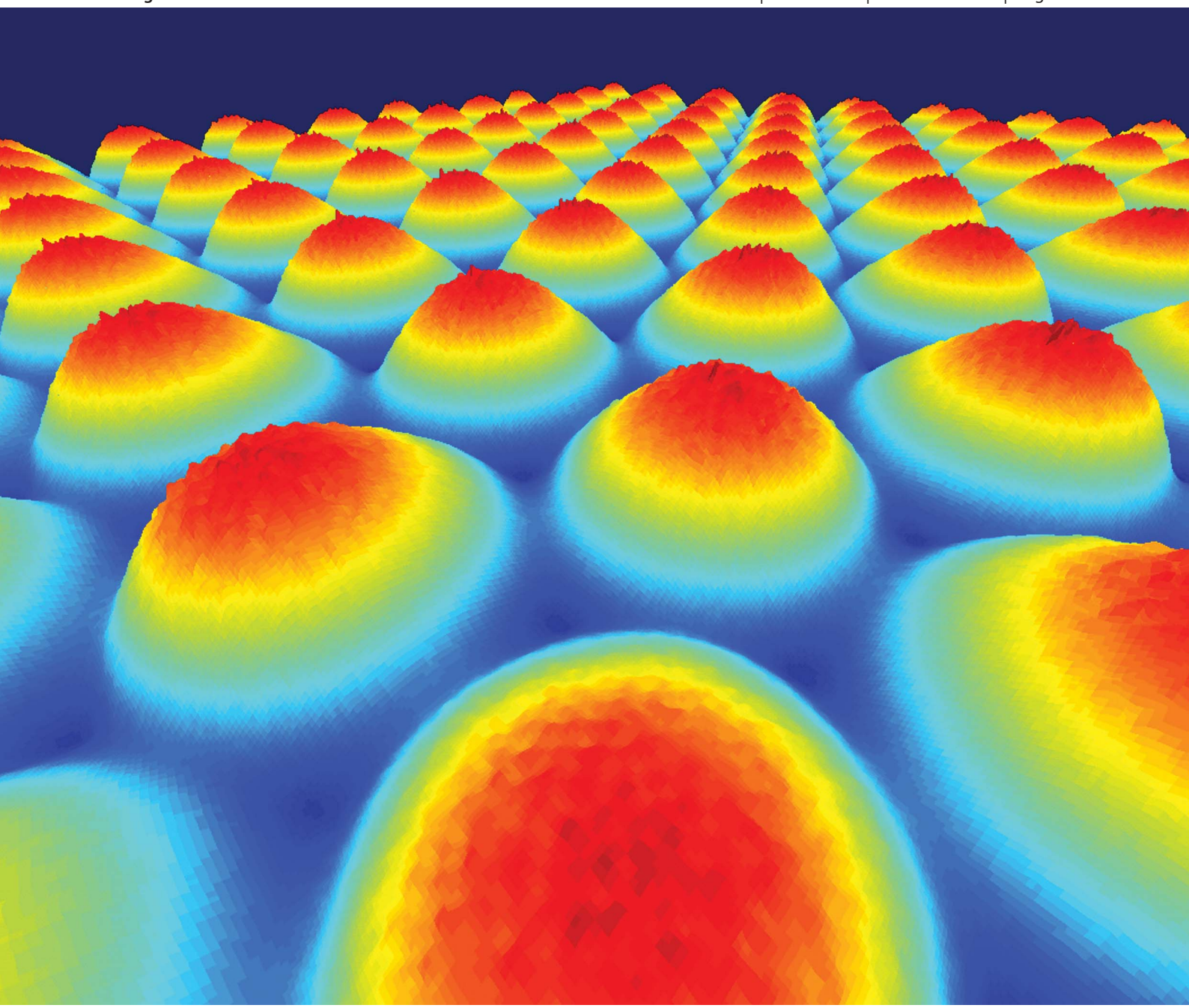

ISSN 1744-683X

RSC Publishing

PAPER

Penger Tong *et al.*

Colloidal diffusion over a periodic energy landscape

1744-683X(2013)9:37;1-Z

Soft Matter

RSC Publishing

PAPER

View Article Online
View Journal | View Issue

Colloidal diffusion over a periodic energy landscape

Cite this: *Soft Matter*, 2013, **9**, 8826

Xiao-guang Ma,[a] Pik-Yin Lai[b] and Penger Tong*[a]

A two-layer colloidal system is developed for the study of colloidal diffusion over a two-dimensional periodic energy landscape. The energy landscape is made from the bottom layer of colloidal spheres forming a honey-comb crystalline pattern above a glass substrate. The corrugated surface of the bottom colloidal crystal provides a gravitational potential field for the diffusing particles in the top layer. The obtained population probability histogram $P(x, y)$ of the diffusing particles is used to fully characterize the energy landscape $U(x, y)$ *via* the Boltzmann distribution. The dynamical properties of the diffusing particle, such as its escape time t_R and diffusion coefficient D are simultaneously measured from the particle's trajectories. The long-time diffusion coefficients D is found to be in good agreement with the theory for all colloidal samples studied. The experiment demonstrates the applications of this newly constructed colloidal energy landscape.

Received 4th May 2013
Accepted 25th July 2013

DOI: 10.1039/c3sm51240a

www.rsc.org/softmatter

I Introduction

Diffusion over a complex energy landscape is a common problem, which appears in many areas of physics and physical chemistry. In surface science for instance, the motion of atoms adsorbed on a crystal surface (adatoms) under thermal agitations is determined by the electronic interactions with the substrate atoms. Finding the connection between the interaction potential and surface diffusion is essential for understanding the mechanisms of surface migration and crystal growth.[1–3] Another example in cell biology is the lateral diffusion of membrane-bound proteins on a cell membrane. The recent development of fluorescent-based probes[4] and optical microscopy techniques[5] has made the study of an increasing number of molecular and biochemical processes in living cells in real time and at the single molecule level possible.[6,7] Because the membrane-bound proteins constantly interact with other proteins and lipids on the membrane and with the underlying cytoskeleton, the study of the protein diffusion can provide dynamic information about the protein interaction and microstructures surrounding the diffusing protein.[8,9]

The third example is the study of conformational changes in protein folding. It has been well established that the dynamics of protein folding can be thought of as diffusion in a funnel-like high dimensional energy landscape along the reaction coordinates.[10,11] With the newly developed tools such as single molecule force spectroscopy, the unfolding forces can be measured by mechanically stretching a single molecular chain,[12,13] generating quantitative information about the fine structures and corresponding energy scales associated with the stretched chain. Highly hierarchical structures and heterogeneous kinetics are found to be typical characteristics of these complex molecular systems.[14] Further complications, such as non-ergodicity and metastability, are also commonly found in these systems, making the application of the sophisticated statistical mechanics models directly to connect the kinematics with the energetics difficult.[15–17]

Our general understanding of this type of problems can be traced back to over a century ago. The well-known Arrhenius equation,[18–20] $k = (k_0/\nu)e^{-E_b/k_BT}$, was proposed to connect the reaction rate k to the activation energy E_b with k_0 being an attempt frequency and ν^{-1} the Arrhenius pre-factor. While the Arrhenius equation can accurately describe the temperature dependence of the reaction rate, it is nevertheless an empirical relation. Kramers[21] considered the reaction rate problem as a transition over an energy barrier under thermal agitations and derived the Arrhenius equation together with an analytical expression for ν^{-1}. The Arrhenius–Kramers equation thus provides a simple physical picture for a common class of diffusive barrier-crossing problems. It is valid for reactions or transitions involving a larger energy barrier, for example with $E_b/k_BT \gtrsim 6$–7.[22,23] In 1962, Lifson and Jackson (LJ)[24] obtained an exact solution for the one-dimensional (1D) Langevin equation[25] with a periodic interaction potential. With LJ's exact solution, the Arrhenius–Kramers equation can be recovered under the steepest-descent approximation.[26] Recent theoretical development in this area includes the study of the Kramers problem for other forms of potential energy landscapes, such as a multi-well potential with[27–29] and without[30] an external force or a random potential,[31,32] and calculations of other statistical properties of the single particle trajectories beyond the mean reaction rate k.[33] Finding an experimental system in which one can track individual particle trajectories with adequate statistics is, therefore, needed in order to test different theoretical ideas.

[a]*Department of Physics, Hong Kong University of Science and Technology, Clear Water Bay, Kowloon, Hong Kong. E-mail: penger@ust.hk*

[b]*Department of Physics, Center for Complex Systems and Graduate Institute of Biophysics, National Central University, Chungli, Taiwan 320, ROC*

Attempts have been made to use colloidal systems to study the barrier-crossing problem. The colloidal systems offer many advantages over atomic or molecular fluids, because the dynamics of the colloidal particles are slower and can be tracked at the single-particle level with video microscopy.[34] They have served as model systems to study a range of interesting problems in soft matter physics.[35,36] In addition, an external magnetic field or optical tweezers can be readily used to confine the colloidal particles in a regular lattice or to apply a constant force to the colloidal system. An array of optical tweezers, each providing an optical trap to the diffusing particles, was used to study the hydrodynamic drag,[37] enhancement of diffusion under an external force[38,39] and sorting of the particles based on their sizes' difference.[40,41]

In this paper, we report a systematic experimental study of colloidal diffusion over a periodic energy landscape. A close packed monolayer of colloidal spheres forms a periodic gravitational energy landscape, over which a second layer of colloidal particles can freely diffuse. Using the techniques of optical microscopy and particle-tracking, we measure the population probability histogram (pph) $P(x, y)$ of finding a diffusing particle at position (x, y) and construct the energy landscape $U(x, y)$ *via* the Boltzmann distribution. The diffusion dynamics of the individual particles are measured from the particle's trajectories. With the simultaneously obtained energetics and dynamics information, we test the theory and demonstrate the applications of the newly constructed colloidal energy landscape. A primary objective of the paper is to delineate the experimental conditions for the precise measurements of the corrugated energy landscape and its hindering effect on colloidal diffusion.

The remainder of the paper is organized as follows. We first describe the theory about the 1D diffusion over a periodic energy landscape in Section II. The experimental procedures and image processing methods are presented in Section III. The experimental results and discussion are given in Section IV. Finally, the work is summarized in Section V.

II Theoretical background

The motion of a Brownian particle can be described by the Langevin equation[25]

$$M\frac{\mathrm{d}^2\vec{r}}{\mathrm{d}t^2}+\xi\frac{\mathrm{d}\vec{r}}{\mathrm{d}t}=f_{\mathrm{B}}(t)-\nabla U(\vec{r}) \quad (1)$$

where $\vec{r}(t)$ is the particle's position at time t, M is its mass, $\xi\frac{\mathrm{d}\vec{r}}{\mathrm{d}t}$ is the drag force experienced by the particle with ξ being the friction coefficient, and $f_{\mathrm{B}}(t)$ is the random Brownian force due to thermal fluctuations of the surrounding fluid. While the mean value of $f_{\mathrm{B}}(t)$ is zero, its autocorrelation function $C(\tau)$ is non-zero and has a form,[42]

$$C(\tau)\equiv\langle f_{\mathrm{B}}(t+\tau)f_{\mathrm{B}}(t)\rangle=2k_{\mathrm{B}}T\xi\delta(\tau) \quad (2)$$

where $k_{\mathrm{B}}T$ is the thermal energy of the system and $\delta(t)$ is the δ-function. The last term, $-\nabla U(\vec{r})$, is the external force acting on the particle resulting from an energy landscape $U(\vec{r})$.

For one-dimensional (1D) cases $[\vec{r}(t)\equiv x(t)]$, analytical solutions were obtained for three simple potentials including $U(x)=0$, $U(x)=-Fx$ and $U(x)=(1/2)kx^2$.[33] Lifson and Jackson (LJ)[24] obtained a general solution of eqn (1) for a periodic potential $U(x)=U(x+\lambda)$ in 1D. Using this solution, they calculated $\bar{t}_N$, which is the mean time taken for a diffusing particle starting at the origin $x=0$ to arrive at either one of the boundaries $\pm N\lambda$ for the first time,

$$\bar{t}_N=\frac{(N\lambda)^2}{2D_0}\left\langle \mathrm{e}^{U(x)/k_{\mathrm{B}}T}\right\rangle_\lambda\left\langle \mathrm{e}^{-U(x)/k_{\mathrm{B}}T}\right\rangle_\lambda, \quad (3)$$

where N is an integer, $\langle\ldots\rangle_\lambda$ denotes an average over the period λ, and $D_0=k_{\mathrm{B}}T/\xi$ is the Stokes–Einstein free diffusion coefficient in the absence of any energy landscape. For a large value of N, the result is independent of the origin and thus one obtains the effective diffusion coefficient,

$$D\equiv\frac{(N\lambda)^2}{2\bar{t}_N}=\frac{D_0}{\left\langle \mathrm{e}^{U(x)/k_{\mathrm{B}}T}\right\rangle_\lambda\left\langle \mathrm{e}^{-U(x)/k_{\mathrm{B}}T}\right\rangle_\lambda}. \quad (4)$$

The hindering effect caused by the potential $U(x)$ is included in the denominator on the right-hand side of eqn (4). The LJ's derivation can also be applied to a double-well potential $U(x)$ with $x=0$ and $x=\lambda$ being its two local minima. With the starting point being set at $x=0$ and $x=\lambda$ being the only boundary, the LJ's derivation gives the mean-first-passage-time (MFPT),[26]

$$\bar{t}_m\simeq t_0\left\langle \mathrm{e}^{U(x)/k_{\mathrm{B}}T}\right\rangle_\lambda\left\langle \mathrm{e}^{-U(x)/k_{\mathrm{B}}T}\right\rangle_\lambda, \quad (5)$$

where $t_0=\lambda^2/D_0$ can be thought as an attempt time in a flat potential field. Thus the transition rate from $x=0$ to $x=\lambda$ in the double-well potential is

$$k\equiv\frac{1}{\bar{t}_m}=\frac{k_0}{\left\langle \mathrm{e}^{U(x)/k_{\mathrm{B}}T}\right\rangle_\lambda\left\langle \mathrm{e}^{-U(x)/k_{\mathrm{B}}T}\right\rangle_\lambda}, \quad (6)$$

where $k_0=1/t_0$ is the attempt rate in a flat potential field. The hindering effect for the diffusion dynamics contains the same factor, $\langle \mathrm{e}^{U(x)/k_{\mathrm{B}}T}\rangle_\lambda\langle \mathrm{e}^{-U(x)/k_{\mathrm{B}}T}\rangle_\lambda$, in both the time and rate representations.

The 1D results can be extended to diffusion on a 2D lattice or even a 3D lattice, if the particle trajectories consist of multiple steps of transitions between the nearest neighbor sites through a quasi-1D passage.[31,43] In this case, the diffusion coefficient D can be expressed in terms of the transition rate k between the nearest neighbor sites:

$$D=\left(\frac{z}{D_{\mathrm{im}}}\right)\frac{k\lambda^2}{2} \quad (7)$$

where z is the number of the nearest neighbor sites in the lattice, D_{im} is the dimension of the lattice and λ is the lattice constant. For a 1D periodic potential where $z=2$ and $D_{\mathrm{im}}=1$, eqn (7) becomes the same as eqn (4). For a 2D honey-comb lattice to be used in the experiment, where each site has 3 nearest neighbors ($z=3$), the effective diffusion coefficient becomes

$$D=\frac{3}{4}\frac{D_0}{\left\langle \mathrm{e}^{U(x)/k_{\mathrm{B}}T}\right\rangle_\lambda\left\langle \mathrm{e}^{-U(x)/k_{\mathrm{B}}T}\right\rangle_\lambda}. \quad (8)$$

Except a numerical factor 3/4, eqn (8) remains the same as eqn (4).

In many practical applications, complete information about $U(x)$ is not available and one is interested in finding the energy barrier height E_b from the measured particle diffusion. When the barrier height $E_b \gg k_BT$, one may use the steepest-descent approximation to calculate $\langle e^{U(x)/k_BT}\rangle_\lambda \langle e^{-U(x)/k_BT}\rangle_\lambda$ and the final result is:[26]

$$\left\langle e^{U(x)/k_BT}\right\rangle_\lambda \left\langle e^{-U(x)/k_BT}\right\rangle_\lambda \simeq \frac{2\pi k_BT}{\left(U_0''\left|U_b''\right|\right)^{1/2}\lambda^2} e^{E_b/k_BT}, \quad (9)$$

where $U_0'' = U''(x = \pm\lambda/2)$ and $U_b'' = U''(x = 0)$ are, respectively, the second derivatives of $U(x)$ at the energy minimum $x = \pm\lambda/2$ and at the energy barrier $x = 0$. Combining eqn (9) and (4), one has

$$\frac{D_0}{D} = \frac{4}{3}\nu e^{E_b/k_BT}, \quad (10)$$

where $\nu = 2\pi k_BT/[(U_0'|U_b'|)^{1/2}\lambda^2]$ is the (reciprocal) Arrhenius pre-factor, and eqn (10) is called the Arrhenius–Kramers equation.[20,21] In the experiment described below, we will examine the validity of eqn (4), (8) and (10).

III Experiment

A Apparatus and sample preparation

Fig. 1 shows the sample cell used in the experiment. A central hole of 6 mm in diameter and 1 mm in depth is drilled through the center of a circular stainless steel cell (SC). The cell has a circular chamber of a slightly larger diameter surrounding the hole and is sealed from the bottom by a glass cover slip (GC). The entire sample cell has two fluid chambers; the central hole is used to hold the colloidal sample and the outer surrounding chamber contains additional solvent (water with the same salt concentration) to prevent sample evaporation. The central hole is first filled with the colloidal sample and is covered by a glass cover slip (GC). Under the action of capillary forces, the contact gap between the top cover slip and central sample cell (both are hydrophilic) is sealed by the sample solvent. The outer chamber is then filled with additional solvent, keeping the central sample chamber from being in contact with the outside air. In this way, sample evaporation is minimized so long as there is some solvent remained in the outer chamber. Extra solvent is added to the outer chamber from time to time during the experiment using an embedded syringe.

The sample cell is placed on the stage of an inverted microscope (Leica DM-IRB), and the motion of the particles is viewed from below using bright field microscopy. Movies of particle motion are recorded using a monochrome CCD camera (CoolSNAP, Media Cybernetics) and streamed to the hard drive of a host computer. They are taken at 7 frames per second. The commercial image acquisition software (ImagePro, Media Cybernetics) is used to control the camera. The recorded images have a spatial resolution of 1392 × 1040 pixels and 256 gray scales.

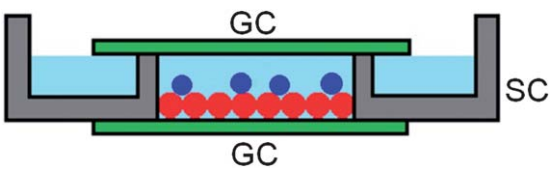

Fig. 1 Schematic diagram of the sample cell (side view): SC, stainless steel cell; GC, glass cover slip; red particles, large silica spheres forming a monolayer crystal on the bottom glass substrate and blue particles, smaller diffusing particles on top of the colloidal crystal.

Plain silica spheres used in the experiment are purchased from Bangs Laboratories (particles with diameter d = 2.1, 3.0 and 3.5 μm) and Corpuscular Inc. (d = 2.9 μm). All the purchased samples are thoroughly washed using deionized water by repeated centrifugation. The original aqueous solution of particles with 5% (g mL^{-1}) solid concentration is diluted by deionized water at a 1 : 100 ratio by weight. The solution is centrifuged at 1000 rpm (at ~100g centrifugal acceleration) for 5 min and the particles settle down to the bottom of the test tube. The supernatant is then removed as much as possible using a pipette and the remaining solid is further diluted by deionized water for a repeated centrifugation. Typically, we repeat this procedure for 8–10 times to make sure that all the impurities in the solution are removed. To further remove particle aggregates from the cleaned solution, we fill the solution in a thin test tube for free sedimentation until the interface between the supernatant and particle-containing solution falls to within 1/2 of the original height. Then we pipette out a small amount of the solution just below the interface. The selected solution is found to contain only the monodisperse particles.

To prepare a close-packed monolayer of colloidal spheres near the water–glass interface, we add the colloidal solution into the sample cell one drop (~200 μL) at a time until the area fraction n occupied by the silica spheres in the bottom layer reaches $n \simeq 0.7$. This process is monitored in real-time with a camera on the microscope and the particles take 1–2 minutes to settle on the glass substrate. The image analysis software ImagePro is used to calculate the area fraction n. Then a 1 mL syringe is used to continue the addition process with a smaller drop (10–20 μL) of the particle solution at a time until n approaches the packing limit $n \simeq 0.8$. The sample is then left open for complete evaporation of water in the solution and the remaining particles are attached to the glass substrate by van der Waals forces. The evaporation process takes several hours to complete at room temperature with a relative humidity of ~70%.

Fig. 2(a) shows a microscopic image obtained using a 10× objective of the monolayer colloidal crystal formed on the glass substrate. Single-crystal patches of size larger than 60 μm are clearly observable and they are separated by grain boundaries. Fig. 2(b) is a magnified image obtained by using a 40× objective, which clearly reveals the hexagonal ordering of the silica spheres and some point defects. By laterally moving the sample stage, we are able to find a single-crystal patch within the view area of 100 × 75 μm^2, which is achieved by using a 63× oil objective together with an extra 1.5× built-in magnifier.

After the formation of the first (dry) layer of silica spheres on the glass substrate, we fill the sample cell with a 0.1 mM aqueous solution of NaCl followed by addition of a drop of colloidal suspension into the aqueous solution using a 1 mL

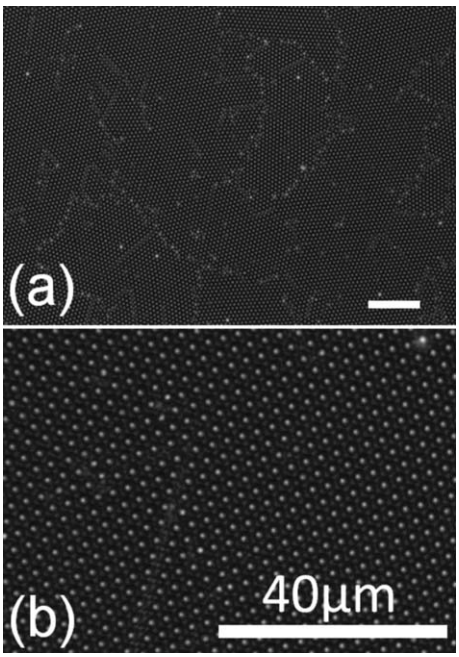

Fig. 2 Microscopic images of the monolayer colloidal crystal made of silica spheres of 2.9 μm in diameter and formed on the glass substrate. The images are obtained using (a) a 10× objective and (b) a 40× objective. The scale bars are the same (40 μm).

syringe. After several minutes, the silica spheres settle down on top of the first layer of the colloidal crystal, and the particle number in the view area is counted by ImagePro. This procedure is repeated until a desired area fraction n for the second layer particles is reached. The sample cell is then covered with a glass cover slip to prevent evaporation. The first (non-mobile) layer of the colloidal crystal provides a rugged surface with ordered bumps and valleys on the surface. As a result, the diffusing particles in the second layer experience a periodic gravitational energy landscape $U(x, y)$.

The value of $U(x, y)$ is controlled by the size of the particles in both layers, which determines the standing height of the second layer particles, and the buoyant mass of the diffusing particles. In addition, there is a small gap between the two layers of silica spheres, which affects both the diffusion dynamics of the particles in the second layer and the energy landscape $U(x, y)$. In the experiment, we keep the gap distance constant by using the 0.1 mM aqueous solution of NaCl to control the Debye screening length of the silica spheres. To vary $U(x, y)$, we prepare seven colloidal samples using silica spheres of different sizes in both top and bottom layers. The seven colloidal samples with different top/bottom particle sizes are listed in Table 1.

B Video microscopy and image analysis

Fig. 3(a) shows silica spheres of 2.14 μm in diameter (bright spots with a non-uniform intensity profile) diffusing over a monolayer colloidal crystal (honey-comb lattice) made of silica spheres of 2.90 μm in diameter (Sample S1). The image is taken with the focal plane located in between the two layers of silica spheres so that the out-of-focus image of the bottom colloidal

Table 1 Seven colloidal samples used in the experiment with different top/bottom particle sizes and the obtained energy landscape parameters, including lattice constant λ, energy barrier height E_b/k_BT, and $R \equiv \langle e^{U(x)/k_BT}\rangle_\lambda \langle e^{-U(x)/k_BT}\rangle_\lambda$, the normalized reciprocal diffusion coefficient D_0/D and the (reciprocal) Arrhenius pre-factor ν (see the text).

Samples	Top/bottom (μm)	λ (μm)	E_b/k_BT	R	D_0/D	ν
S1	2.1/2.9	1.7	1.5	1.3	1.5	0.26
S2	2.1/3.5	2.0	1.6	1.5	2.2	0.13
S3	2.9/2.9	1.7	3.3	3.0	4.4	0.07
S4[a]	2.9/2.9	1.9	3.7	4.3	5.3	0.064
S5	2.9/3.0	1.7	3.6	3.7	5.8	0.055
S6	2.9/3.5	2.0	4.8	9.3	10.8	0.05
S7	3.5/3.5	2.0	6.4	30.4	46	0.04

[a] Particles on the bottom layer are also mobile.

crystal becomes a honey-comb lattice and the top diffusing particles appear as bright spots. The center of the hexagons corresponds to the center of the spheres in the bottom layer. The background pattern provides a convenient coordinate system for the rugged surface, on which one can determine the occupation statistics of the diffusing particles.

The non-uniform intensity profile of the diffusing particles is caused by the interference with the bottom layer particles. By applying a standard Gaussian image filter from the Matlab image process toolbox, one can recover the uniform Gaussian-like intensity profile for each diffusing particle, as shown in Fig. 3(b). The central position of the intensity profile

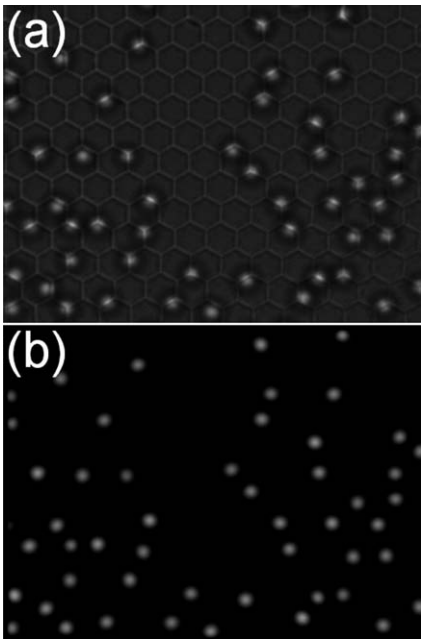

Fig. 3 (a) Microscopic image of Sample S1. The uniform honey-comb pattern in the background is the interference pattern resulting from the bottom layer colloidal crystal. The bright dots with a non-uniform intensity profile are the diffusing particles in the top layer. (b) After removal of the background pattern using a Gaussian image filter, the bright dots with a uniform intensity profile represent the diffusing particles on a uniform black background.

is thus chosen as the center of the diffusing particle. With this method we are able to obtain a repeatable tracking accuracy of ~1 pixel, which is 49 nm. A homemade program based on the standard tracking algorithm[34] is used to track the trajectory of the diffusing particles from consecutive images. Fig. 8 below shows an example of two simultaneously tracked 1 h-long particle trajectories consisting of more than 2×10^4 consecutive steps.

For long-time particle tracking and accumulation of the particle's occupation histogram, one has to correct small lateral drifts of the sample cell relative to the microscope objective, which occur occasionally due to the relaxation of some mechanical component of the microscope, such as the sample stage. In the experiment, we use the frozen background pattern as a reference to calculate the drift displacement in each image relative to the first one and then subtract it out from all the particle positions. This is accomplished by calculating the two-dimensional spatial correlation function

$$C(x,y) = \frac{\sum_i \sum_j (A_{ij} - \overline{A})(B_{ij} - \overline{B})}{\sqrt{\left[\sum_i \sum_j (A_{ij} - \overline{A})^2\right]\left[\sum_i \sum_j (B_{ij} - \overline{B})^2\right]}}, \quad (11)$$

where A and B are two $i \times j$ image matrices obtained from the same cropped sub-area at two different times. Because the positions of the diffusing particles on the top layer are randomly distributed in each image, their images (bright spots in Fig. 3) contribute little to $C(x, y)$. The bright pattern of the frozen colloidal crystal on the bottom layer is fixed in space, and its drift in time will cause the peak value of $C(x, y)$ to occur at a location $(x, y)_{\text{peak}} \neq 0$. The resulting displacement vector $(x, y)_{\text{peak}}$ is then subtracted out from all the particle positions in each image. In this way, any drift distance smaller than the repeating unit of the colloidal crystal (lattice constant $\lambda = 30$ pixels) can be uniquely determined throughout our experiment.

IV Experimental results

A Energy landscape

To find the occupation statistics of the diffusing particles over the rugged surface, we add 5×10^4 images together, each containing ~150 particles, and compute the number of particles in each pixel area. In this way we obtain the population probability histogram (pph) $P(x, y)$ of finding a diffusing particle at a location (x, y), which is related to the gravitational energy landscape $U(x, y)$ of the rugged surface *via* the Boltzmann distribution,

$$P(x, y) \sim e^{-U(x,y)/k_B T}. \quad (12)$$

Eqn (12) is valid when the surface coverage of the particles is low so that the occupation statistics are not affected by the crowding effect at finite particle concentrations. In the experiment, we measure $P(x, y)$ at two area fractions, $n = 0.15$ and $n = 0.3$, and no visible difference is found in the two pphs. Hereafter, all the measured $P(x, y)$ are obtained at $n \simeq 0.15$.

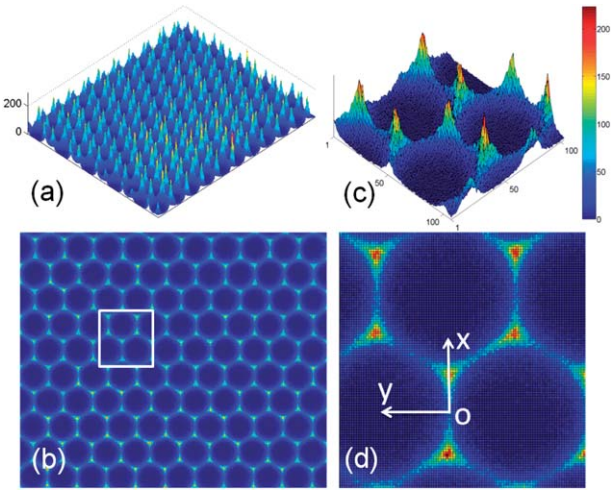

Fig. 4 (a) 3D plot of the measured pph $P(x, y)$ of finding a diffusing particle at a location (x, y) for Sample S1; (b) top view of the measured $P(x, y)$; (c) an enlarged 3D plot of $P(x, y)$ over a small area drawn by a white square in (b) and (d) top view of the measured $P(x, y)$ in (c).

Fig. 4(a) shows a 3D plot of the measured $P(x, y)$ over a large area for Sample S1. Fig. 4(b) is the top view of the measured $P(x, y)$, showing the same hexagonal structure as the background pattern shown in Fig. 3(a). The peak positions of the measured $P(x, y)$ are located at the interstices (valleys) of the 2D colloidal crystal. The shape and symmetry of the measured $P(x, y)$ reflect the geographic variations of the underlying rugged surface. Fig. 4(c) shows an enlarged 3D plot of $P(x, y)$ over a small area drawn by a white square in Fig. 4(b). Fig. 4(d) shows a top view of the measured $P(x, y)$ in Fig. 4(c). Fig. 4(c) reveals more structural details including number fluctuations in the measured $P(x, y)$, which are caused by the limited statistics due to a finite number of particles in certain locations. To quantitatively describe $P(x, y)$, we choose a coordinate system as shown in Fig. 4(d). The relative error $\sigma(x, y)$ of the measured $P(x, y)$ can be estimated as $\sigma(x, y) = 1/\sqrt{n_i(x, y)}$, where $n_i(x, y)$ is the number of particles counted in the i^{th} pixel. Typically, we have ~200 particles in the peak region of $P(x, y)$, which gives $\sigma_{\text{peak}} \simeq 14\%$. In the valley regions of $P(x, y)$, σ_{valley} can be as large as $\sigma_{\text{valley}} \simeq 30\%$, corresponding to an energy uncertainty of $\pm 0.3\ k_B T$.

To further improve the statistical accuracy of $P(x, y)$, we take advantage of the spatial periodicity of $P(x, y)$ and divide the measured $P(x, y)$ over the entire area into unit cells, each containing only one peak at the cell center. The measured $P(x, y)$'s in these unit cells are added together with correct symmetry and we obtain the final $P_s(x, y)$ with super statistical accuracy. Fig. 5(a) shows a 3D plot of the resulting $P_s(x, y)$ for Sample S1. Fig. 5(b) is the top view of $P_s(x, y)$, showing the three-fold symmetry of the underlying energy landscape. Note that the number of particles counted at the peak position of $P_s(x, y)$ has increased by more than 100 times. The envelope of the probability peak now is much smoother compared with those shown in Fig. 4(c). With such a high statistical accuracy, we estimate the relative error of $P_s(x, y)$ at position O to be $\sigma_{\text{valley}} \lesssim 3\%$. In obtaining $P_s(x, y)$, we have removed the data in the defect areas of the colloidal crystal.

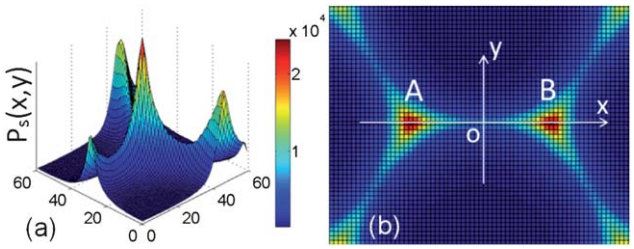

Fig. 5 (a) 3D plot of $P_s(x, y)$ averaged over more than 100 periodic areas and (b) top view of the measured $P_s(x, y)$ for Sample S1.

Fig. 6(a) shows the measured $P_s(x, y)$ as a function of x for four different values of y. The measured pphs are all symmetric about the saddle point $x = 0$, having two peaks symmetrically located at the two valley regions of the 2D colloidal crystal (A and B). The pph curve $P_s(x, y = 0)$ (black squares) shows the two highest probability peaks, which decay gradually as the position of y moves away from the symmetric line at $y = 0$ on both sides. When a particle moves from one valley region (say A) to another valley region (say B), it has to crossover a barrier region located around the origin O, at which $P_s(x, y)$ takes its minimum value. This barrier region shapes like a narrow channel connecting A and B, along which the particles hop back and forth.

Fig. 6(b) shows the cross-sectional view of the narrow channel, *i.e.*, $P_s(x, y)$ as a function of y, at three different locations of x. While the measured pph curves $P_s(x, y)$ along the narrow channel have different amplitudes, they share the same functional form independent of the values of x. Fig. 6(c) shows the normalized pph $P_n(x, y) = P_s(x, y)/P_s(x, y = 0)$ as a function of y for three different values of x. All the curves collapse onto a single master curve, suggesting that $P_s(x, y)$ as a function of y indeed has a uniform shape. If we denote this uniform envelop function as $P_n(y) \equiv p_n(x, y)$, the measured $P_s(x, y)$ can be written as $p_s(x, y) = p_n(y)p_s(x, y = 0)$. Such a decoupling of the 2D pph into a product of two 1D functions allows one to approximate the particle's motion as a quasi-1D motion from A to B (or B to A) within a narrow channel, whose shape is described by $P_n(y)$. The full width at half maximum (FWHM) of $P_n(y)$ is 6.2 pixels (=0.3 μm), which is small compared with the channel length ($\simeq$ 1.7 μm).

With eqn (12) we calculate the quasi-1D energy landscape, $U(x)/k_BT = -\ln P_s(x, y = 0)$, where $P_s(x, y = 0)$ is normalized in such a way that $U(x) = 0$ at the local energy minimum. Fig. 7(a) shows the resulting $U(x)/k_BT$ as a function of x for seven different samples. The unit of x has been converted from pixel to micrometer using 1 pixel = 49 nm for our microscope. The separation between the two local energy minima is determined by the lattice constant $\lambda = d/\sqrt{3}$ of the underlying colloidal crystal (except for Sample S4, which will be discussed in Section IV(C)). Here d is the diameter of the particles in the bottom layer. It is seen that the energy barrier height E_b varies in the range of 1.5–6.4 k_BT among the seven samples. The values of the measured λ and E_b are given in Table 1.

It is found that the normalized energy landscape $U(x)/E_b$ has a universal form once x is normalized by λ. Fig. 7(b) shows the measured $U(x)/E_b$ as a function of the normalized distance $x^* = x/\lambda$. Indeed, the seven different energy landscapes as shown in Fig. 7(a) collapse onto a single master curve once they are plotted in the normalized way as shown in Fig. 7(b). As discussed in Section III(A), the barrier height E_b is determined by the size of the particles in both top and bottom layers.

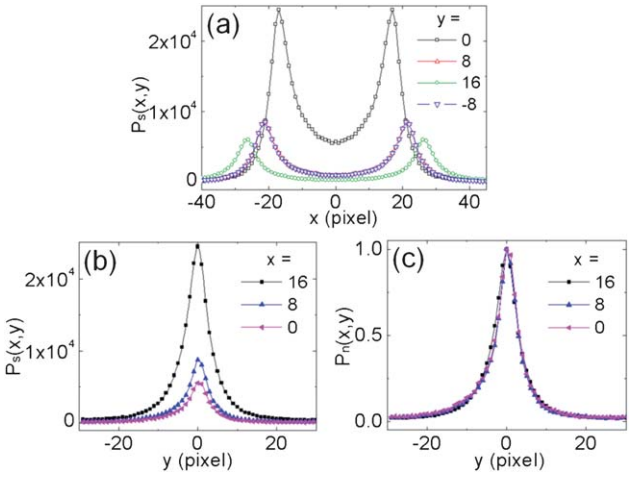

Fig. 6 (a) Measured $P_s(x, y)$ as a function of x for four different values of y: y = 0 (black squares), 8 (red up triangles), 16 (green circles) and −8 (blue down triangles). (b) Measured $P_s(x, y)$ as a function of y for three different values of x: x = 16 (black squares), 8 (blue up triangles) and 0 (pink left triangles). (c) Normalized pph $P_n(x, y)$ as a function of y for three different values of x: $x = 16$ (black squares), 8 (blue up triangles) and 0 (pink left triangles). All numbers are expressed in units of pixels and the solid lines are drawn to guide the eye.

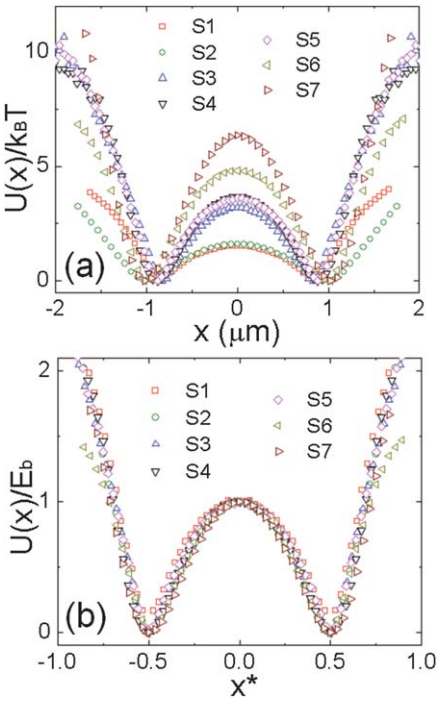

Fig. 7 (a) Measured energy landscape $U(x)/k_BT$ as a function of x for seven different samples; (b) normalized energy landscape $U(x)/E_b$ as a function of the normalized distance $x^* = x/\lambda$.

B Colloidal diffusion over a frozen energy landscape

Fig. 8 shows two 1 h-long trajectories (yellow and pink) of the diffusing particles over the bottom colloidal crystal for Sample S1. The background honey-comb lattice reveals the structure of the bottom colloidal crystal. From the central positions of the bottom lattice sites, which coincide with the peak positions of the measured $P(x, y)$, we can divide the view area into numbered unit cells and find which cell the diffusing particle belongs to at a given time. In this way, the particle's trajectory is transformed from a time series of continuous spacial positions to a time series of numbered lattice sites. From this time series, we measure the residence time t_R (which is also called 'dwell time' or 'escape time') for each diffusing particle to stay in a lattice site by finding the trajectory length during which it belongs to this site. Because the diffusing particles spend more time in the central valley regions of the bottom lattice, one can measure t_R with better statistics.

Fig. 9 shows the histogram $H(t_R)$ of the residence time t_R obtained from the particle trajectories in Sample S1. The measured $H(t_R)$ has a long tail, which is well described by a simple exponential function, $H(t_R) = 900\exp(-t_R/5)$ (solid line). This suggests that the escape events occur randomly in time and thus can be described by a Poisson process with an exponential distribution in $H(t_R)$.[26] A slight curve-up in the measured $H(t_R)$ for small values of t_R is caused by small variations (2–5%) in lattice periodicity of the bottom colloidal crystal. Such deviations give rise to errors in defining the actual boundary of the unit cell at the peak position of the energy barrier. From the measured $H(t_R)$, one can calculate the mean value of t_R as $\bar{t}_R = \sum t_R H(t_R)/\sum H(t_R)$. The measured $\bar{t}_R$ for our samples spans two decades from ~5 s for Sample S1 to ~600 s for Sample S7.

For short times, the particles diffuse mostly in the local minimum of a lattice site. After staying inside the site for a time period t_R, the particle will escape to the nearest neighbor site. The mean escape time (or residence time) $\bar{t}_R$ is related to the mean-first-passage-time (MFPT) $\bar{t}_m$ in eqn (5) *via* the equation[26]

$$\bar{t}_R = \frac{\bar{t}_m}{z} = \frac{t_0}{z}\left\langle e^{U(x)/k_BT}\right\rangle_\lambda \left\langle e^{-U(x)/k_BT}\right\rangle_\lambda, \quad (13)$$

where z is the number of the nearest neighbor sites in the lattice, and for a 2D honey-comb lattice one has $z = 3$.

From the measured $U(x)$ for different samples as shown in Fig. 7(a), we numerically calculate the integral $\langle e^{U(x)/k_BT}\rangle_\lambda \langle e^{-U(x)/k_BT}\rangle_\lambda$ and the final results are given in Table 1. Fig. 10 shows a comparison between $\bar{t}_R/t_0$ and $\langle e^{U(x)/k_BT}\rangle_\lambda \langle e^{-U(x)/k_BT}\rangle_\lambda$. In the plot, we have used $t_0 = \lambda^2/D_0$, where the lattice constant λ is obtained from the particle imaging and the free diffusion coefficient D_0 is measured on a flat surface for each colloidal sample. The solid line is a plot of eqn (13) with $z = 3$, which agrees well with the experimental results.

From the particle trajectories, one can also calculate the mean square displacement (MSD) $\langle \Delta r^2(\tau)\rangle$ as a function of delay time τ, where $\Delta\mathbf{r} = \mathbf{r}(t + \tau) - \mathbf{r}(t)$. Fig. 11 shows log–log plots of the measured MSD $\langle \Delta r^2(\tau)\rangle$ as functions of τ for seven different samples. The two arrows point to the positions at which $\tau = \bar{t}_R$ for S1 and S7. The MSD curve can be generally described by the equation, $\langle \Delta r^2(\tau)\rangle \sim \tau^\gamma$, where the exponent γ is used to classify the particle's motion as normal diffusion ($\gamma = 1$), sub-diffusion ($\gamma < 1$) or super-diffusion ($\gamma > 1$). It is found that for $\tau < \bar{t}_R$, the particles move in and out of a local energy minimum and their motion is sub-diffusive with $\gamma < 1$. For $\tau > \bar{t}_R$, the particles hop among different energy barriers and their motion becomes random diffusive with $\gamma = 1$. The solid line indicates a power-law of slope unity. In this case, one obtains the self diffusion coefficient D from the slope of the MSD curve *via* $D = \langle \Delta r^2(\tau)\rangle/4\tau$. Presumably, for $\tau \ll \bar{t}_R$, the particles will rattle around in a local energy minimum and one should observe free diffusion with

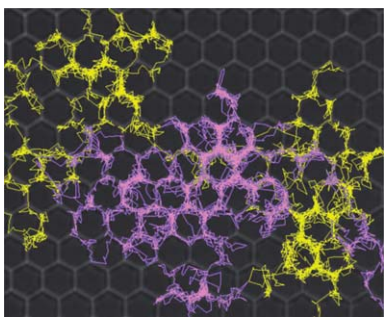

Fig. 8 Two 1 h-long trajectories (yellow and pink) of the diffusing particles over the bottom colloidal crystal for Sample S1.

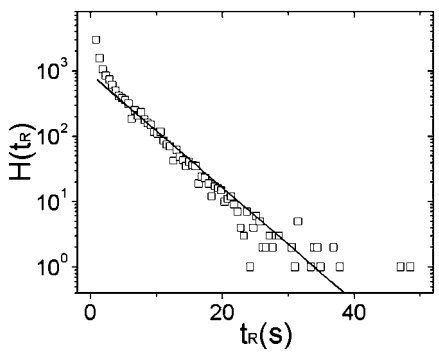

Fig. 9 Measured histogram $H(t_R)$ of the residence time t_R for Sample S1. The solid line is an exponential fit, $H(t_R) = 900\exp(-t_R/5)$, to the tail part of the measured $H(t_R)$.

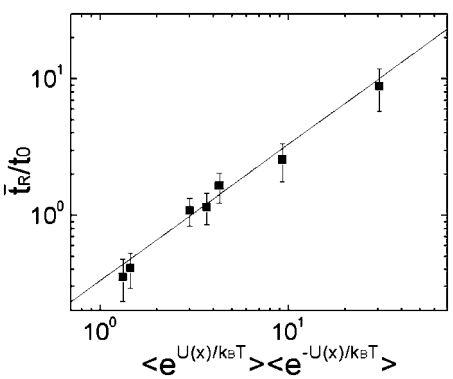

Fig. 10 Comparison between the measured $\bar{t}_R/t_0$ and $\langle e^{U(x)/k_BT}\rangle_\lambda \langle e^{-U(x)/k_BT}\rangle_\lambda$ in log–log scales. The solid line is a plot of eqn (13) with $z = 3$.

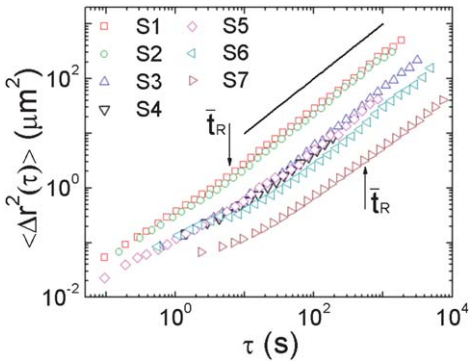

Fig. 11 Log–log plots of the measured MSD $\langle \Delta r^2(\tau) \rangle$ as functions of delay time τ for seven different samples. The solid line indicates a power-law of slope unity. The two arrows point to the positions at which $\tau = \bar{t}_R$ for S1 and S7.

$\gamma = 1$. While it would be interesting to study the transition between the two diffusive regimes, the focus of the present study is on the long-time behavior of the measured MSD.

Fig. 12 shows the measured self-diffusion coefficient $D(n)$ as a function of the area fraction n occupied by the particles. In the plot, $D(n)$ is normalized by its value $D(0)$ measured at the dilute limit $n \simeq 0.04$. Data from four different samples are shown. They are $d = 1.57$ μm and $d = 2.14$ μm particles diffusing over a crystal lattice made by $d = 2.90$ μm silica spheres (1.57/2.90 and 2.14/2.90, solid symbols) and $d = 1.57$ μm and $d = 3.01$ μm particles diffusing over a flat glass surface (1.57/flat and 3.01/flat, open symbols). All the measured $D(n)/D(0)$ curves decrease linearly with n and they collapse to two master curves. The open symbols for diffusion over a flat glass surface can be well described by the equation, $D(n)/D(0) = 1 - \alpha n$, with $\alpha = 1.2$ (dashed line). The solid symbols for diffusion over a frozen colloidal crystal (an energy landscape) can also be well described by the same equation but with a larger slope $\alpha = 1.6$ (solid line).

While at the moment we do not have a theory to quantitatively explain the observed n-dependence of $D(n)$, it is known[44,45] that colloidal suspensions are not a continuum and the individual spheres feel a local viscosity which is different from its macroscopic counterpart. In this case, the hindering of the particle's motion with increasing n is mainly caused by the hydrodynamic interactions (HIs) between the diffusing particles.[35,46,47] This is true for dilute and moderately concentrated suspensions. For very large values of n, direct thermodynamic interactions between the particles also play a role. It is interesting to see from Fig. 12 that the effect of HIs seems to be enhanced by the rugged surface of the underlying colloidal crystal.

We now focus on the effect of the energy landscape on the diffusion coefficient $D \equiv D(0)$ measured at the dilute limit ($n \simeq 0.04$). Fig. 13 shows a comparison between the normalized reciprocal diffusion coefficient D_0/D and $\langle e^{U(x)/k_BT} \rangle_\lambda \langle e^{-U(x)/k_BT} \rangle_\lambda$. Here D_0 is the diffusion coefficient measured on a flat glass surface with the same diffusing particles from each sample. The solid line is a plot of eqn (8), which agrees well with the experimental results. By comparing Fig. 10 and 13, we find that $D = \lambda^2/(4\bar{t}_R)$ [see eqn (5), (8) and (13)].

In calculating the integral $\langle e^{U(x)/k_BT} \rangle_\lambda \langle e^{-U(x)/k_BT} \rangle_\lambda$, one has to know the functional form of $U(x)$. In many applications, however, complete information about $U(x)$ is not known and one is interested in finding the energy barrier height E_b from the measured particle diffusion. Fig. 14(a) shows the measured $D_0/(\nu D)$ as a function of E_b/k_BT. In this plot, the effect of the Arrhenius pre-factor ν has been divided out in the vertical axis. We compute the values of ν for different E_b values using the measured $U(x)$ and the results are given in Table 1. Table 1 reveals that the calculated values of ν decrease with increasing E_b and they seem to converge to a value close to 0.04 for Sample S7 with the largest E_b studied. The solid line in Fig. 14(a) is a plot of eqn (10) with ν being moved to the left-hand side of the equation. It is seen that eqn (10) fits the data quite well especially for the large values of $E_b/(k_BT)$. There is a small but visible systematic deviation between the data and eqn (10) (solid line), which becomes larger for smaller values of $E_b/(k_BT)$ (except for S1). As mentioned in Section II, eqn (10) is obtained by using the steepest-descent approximation, which is known to be accurate only when $E_b/k_BT \gtrsim 6$–7.[22,23] For smaller values of E_b/k_BT, the steepest-descent approximation is not accurate, which explains the deviation observed in Fig. 14(a).

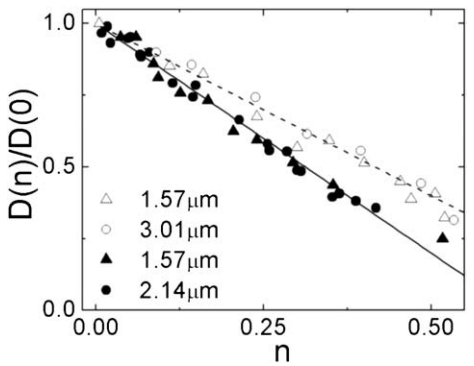

Fig. 12 Normalized diffusion coefficient $D(n)/D(0)$ as a function of the area fraction n for four different samples: 1.57/2.90 (solid triangles), 2.14/2.90 (solid circles), 1.57/flat (open triangles) and 3.01/flat (open circles). The solid and dashed lines show the linear fit, $D(n)/D(0) = 1 - \alpha n$, to the solid and open symbols with $\alpha = 1.6$ and $\alpha = 1.2$, respectively.

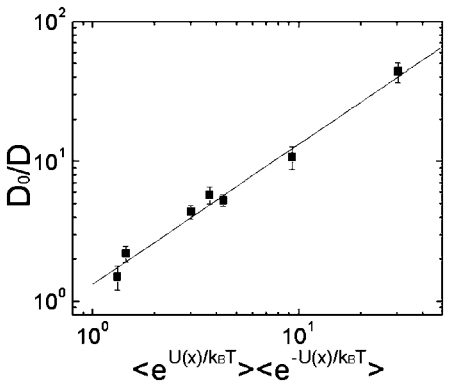

Fig. 13 Comparison between the normalized measured reciprocal diffusion coefficient D_0/D and $\langle e^{U(x)/k_BT} \rangle_\lambda \langle e^{-U(x)/k_BT} \rangle_\lambda$ in log–log scales. The solid line is a plot of eqn (8).

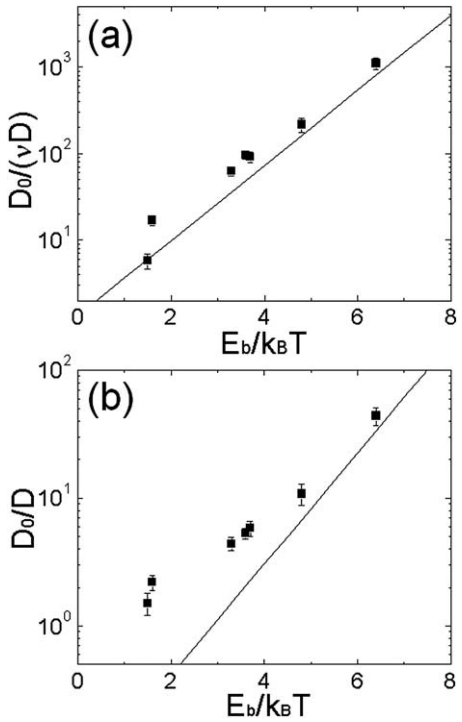

Fig. 14 (a) Measured $D_0/(\nu D)$ as a function of the energy barrier height E_b/k_BT. The solid line is a plot of eqn (10). (b) Measured D_0/D as a function of E_b/k_BT. The solid line is a plot of eqn (10) with $\nu = 0.04$.

Note that to accurately calculate ν, one still needs to know partial information about $U(x)$ (*i.e.*, U_0'' and U_b''). If this information is not known, one can only plot D_0/D as a function of E_b/k_BT as shown in Fig. 14(b). The uncertainties in ln ν will lead to errors in the resulting value of E_b/k_BT. The solid line is a plot of eqn (10) with $\nu = 0.04$. It is seen that there exist deviations between the measured D_0/D (symbols) and the Arrhenius–Kramers equation (solid line). The deviation is larger for small values of E_b/k_BT and the data approach the solid line at the largest value of $E_b/k_BT = 6.4$ studied. For this Sample (S7), we find that the difference between the measured E_b/k_BT and the calculated value using eqn (10) is only 5%.

C Colloidal diffusion over a fluctuating energy landscape

We now consider samples S3 and S4, which are made by the same pair of the top and bottom layer particles. The only difference between S3 and S4 is that for S4 the particles on the bottom layer are not stuck on the substrate and they form a colloidal crystal with the individual particles constantly diffusing around their equilibrium positions. For S3, however, the particles on the bottom layer are stuck on the substrate and the colloidal crystal formed by these particles is a frozen one. During the drying process, the moving contact line between the particle suspension and the dried substrate pushes the silica spheres together and forces them to form a close packed crystal.[48] As a result, the lattice constant of S4 is approximately 12% larger than that of S3 (see Table 1). In addition, the energy barrier height E_b between the two samples is also different.

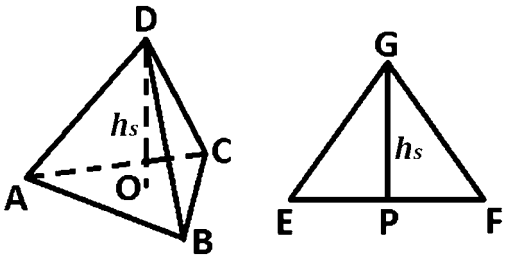

Fig. 15 Packing geometry of the top diffusing particle (D) and (G) standing over the local energy minimum (at $x = \pm\lambda/2$) formed by three triangularly arranged bottom particles (A), (B), and (C) (left tetrahedron) and over the local energy maximum (at $x = 0$) formed by two bottom particles (E) and (F) (right triangle). The altitudes DO and GP represent the standing height $h_s(x)$ at the two locations. The letter symbols used refer to the center of the particles.

As mentioned in Section III(A), E_b is determined by the standing height $h_s(x)$ of the diffusing particle on the second layer along the quasi-1D energy landscape $U(x)$. The functional form of $U(x)$ depends on the diameter d of the particles in both the top and bottom layers, the gap ε_g between the top and bottom layer particles, the gap ε_b between the particles in the bottom layer, and the buoyant mass $\Delta m = (4/3)\pi\Delta\rho(d/2)^3$ of the diffusing particle, where $\Delta\rho$ is the particle's buoyant density in water. For samples S3 and S4, we find

$$E_b = \Delta m g \Delta h_s, \tag{14}$$

where Δh_s is the difference in standing height between the two locations at $x = \pm\lambda/2$ where $U(x)$ is minimum and at $x = 0$ where $U(x)$ reaches its maximum value (see Fig. 7).

Fig. 15 shows the packing geometry of the top and bottom spheres at the local energy minimum ($x = \pm\lambda/2$) (left tetrahedron) and at the local energy maximum ($x = 0$) (right triangle). The altitudes DO and GP represent the standing height $h_s(x)$ at the two locations. The center-to-center distance between two neighboring spheres can be written as AB = BC = CA = $d + \varepsilon_b$, and DA = DB = DC = $d + \varepsilon_g$, where ε_b and ε_g are the corresponding gap distances between the two spheres. Given the packing geometry as shown in Fig. 15, we find

$$h_s(\pm\lambda/2)^2 + \frac{1}{3}(d+\varepsilon_b)^2 = (d+\varepsilon_g)^2, \tag{15}$$

and

$$h_s(0)^2 + \frac{1}{4}(d+\varepsilon_b)^2 = (d+\varepsilon_g)^2. \tag{16}$$

From eqn (15) and (16) we find $\Delta h_s \equiv h_s(0) - h_s(\pm\lambda/2)$ has the form,

$$\Delta h_s = \sqrt{(d+\varepsilon_g)^2 - \frac{1}{4}(d+\varepsilon_b)^2} - \sqrt{(d+\varepsilon_g)^2 - \frac{1}{3}(d+\varepsilon_b)^2} \simeq 0.05d - 0.07\varepsilon_g + 0.12\varepsilon_b. \tag{17}$$

Eqn (17) suggests that Δh_s increases with ε_b monotonically. In the experiment, we find $\varepsilon_b \simeq 0$ for S3 and $\varepsilon_b \simeq d/10$ for S4. Thus the change in E_b between S4 and S3 is expected to be

~20%. From Table 1 we find that the measured E_b for S4 is indeed increased and the amount of increment is ~10%, which is slightly smaller than the above estimation. It should be noted, however, that in the above calculation we have made a number of simplifications about the colloidal samples used in the experiment. For example, we have not considered the effect of polydispersity of the particles in the bottom layer, which may introduce variations in the local particle arrangement. We have also not considered the gravity effect of the top layer particles on the local structure of the bottom colloidal crystal. The gap distance ε_g between the top and bottom layers of silica spheres depends on the sphere's surface charge and Debye screening length in the solution and is not directly measurable in our experiment. However, we used the salt solution to stabilize the Debye screening length of the silica spheres. Given these complexities, we find that direct calculation of the absolute value of E_b for different colloidal systems is not always reliable but eqn (14)–(17) can be used to explain the general trend for a fixed colloidal system.

V Conclusion

We have developed a model system to study the colloidal diffusion in a 2D periodic energy landscape. The energy landscape $U(x, y)$ is made from a monolayer of colloidal particles forming a close packed crystalline pattern above a glass substrate. The corrugated surface of the colloidal crystal provides a gravitational potential field for the diffusing particles on top of the colloidal monolayer. Using the techniques of video microscopy and particle tracking, we obtain the particles' trajectories from more than 10^4 consecutive images. The obtained population probability histogram (pph) $P(x, y)$ of the diffusing particles with a spatial resolution of ~50 nm is used to fully characterize the energy landscape $U(x, y)$ *via* the Boltzmann distribution. The periodic nature of the colloidal crystal allows us to further improve the accuracy of the measured $U(x, y)$ to within ~0.1 k_BT by averaging $P(x, y)$ over the repetitive regions. It is found that the 2D energy landscape can be simplified to an equivalent 1D barrier function $U(x)$ with the barrier height E_b in the range of 1.5–6.4 k_BT.

From the obtained particle trajectories, we measure the escape time t_R of a diffusing particle jumping out of a local energy minimum for the first time. The histogram of t_R is found to have a long exponential tail in accordance with the theoretical expectation. The measured mean square displacement (MSD) of the moving particles becomes diffusive when the lag time is larger than the mean escape time $\bar{t}_R$. The long-time diffusion coefficient D is found to be in good agreement with eqn (8) for all colloidal samples studied. The experiment reveals that the Arrhenius–Kramers equation is accurate when $E_b/k_BT >$ 6.4 as expected. For smaller values of E_b/k_BT, systematic deviations from the experimental results are observed. The Arrhenius–Kramers equation can be extended to smaller values of E_b, when the Arrhenius pre-factor ν can be calculated more accurately.

With the capability of simultaneously tracking the particle's motion and measuring the energy landscape, the colloidal system can serve as a model system to study a range of interesting issues involved in the barrier-crossing problems, such as diffusion over an energy landscape under a constant force and anomalous diffusion in random fields with heterogeneous energy barriers. By increasing the experimental duration, one can achieve a greater accuracy for the energy landscape and a broader range of time scales. This work represents the first step towards these directions.

Acknowledgements

We thank Xuhui Huang for useful discussions. This work was supported in part by the Hong Kong Research Grants Council under Grant no. HKUST-604310 (P.T.) and by the NSC of ROC under the grant no. 101-2112-M-008-004-MY3 (P.Y.L.).

References

1 G. Ayrault and G. Ehrlich, *J. Chem. Phys.*, 1973, **60**, 281.
2 Z. Y. Zhang and M. G. Lagally, *Science*, 1997, **276**, 377.
3 J. Repp, G. Meyer, F. E. Olsson and M. Persson, *Science*, 2004, **305**, 493.
4 L. D. Lavis and R. Raines, *ACS Chem. Biol.*, 2008, **3**, 142.
5 M. Bates, B. Huang and X.-W. Zhuang, *Curr. Opin. Chem. Biol.*, 2008, **12**, 505.
6 M. J. Saxton and K. Jacobson, *Annu. Rev. Biophys. Biomol. Struct.*, 1997, **26**, 373.
7 A. Kusumi, C. Nakada, K. Ritchie, K. Murase, K. Suzuki, H. Murakoshi, R. S. Kasai, J. Kondo and T. Fujiwara, *Annu. Rev. Biophys. Biomol. Struct.*, 2005, **34**, 351.
8 F. Zhang, G. M. Lee and K. Jacobson, *BioEssays*, 1993, **15**, 579.
9 K. Jacobson, E. D. Sheets and R. Simson, *Science*, 1995, **268**, 1441.
10 R. L. Baldwin, *Nature*, 1994, **369**, 183.
11 R. L. Baldwin, *J. Biomol. NMR*, 1995, **5**, 103.
12 S. B. Smith, L. Finzi and C. Bustamante, *Science*, 1992, **258**, 1122.
13 J. Zlatanova, S. M. Lindsay and S. H. Leuba, *Prog. Biophys. Mol. Biol.*, 2000, **74**, 37.
14 R. Nevo, V. Brumfeld, R. Kapon, P. Hinterdorfer and Z. Reich, *EMBO Rep.*, 2005, **6**, 482.
15 H. Frauenfelder, S. G. Sligar and P. G. Wolynes, *Science*, 1991, **254**, 1598.
16 P. G. Wolynes, J. N. Onuchic and D. Thirumalai, *Science*, 1995, **267**, 1619.
17 D. J. Wales, M. A. Miller and T. R. Walsh, *Nature*, 1998, **394**, 758.
18 J. H. Van't Hoff, in *Etudes de Dynamiques Chimiques*, p. 114, (F. Muller and Co., Amsterdam, 1884); translated by T. Ewan, Studies in Chemical Dynamics (London, 1896).
19 W. Ostwald, *J. Prakt. Chem.*, 1884, **30**, 93.
20 S. Arrhenius, *Z. Phys. Chem.*, 1889, **4**, 226.
21 H. A. Kramers, *Physica*, 1940, **7**, 284.
22 J. V. Barth, H. Brune, B. Fischer, J. Weckesser and K. Kern, *Phys. Rev. Lett.*, 2000, **84**, 1732.
23 G. L. Hunter and E. R. Weeks, *Phys. Rev. E: Stat., Nonlinear, Soft Matter Phys.*, 2012, **85**, 031504.

24 S. Lifson and J. L. Jackson, *J. Chem. Phys.*, 1962, **36**, 2410.
25 P. Langevin, *C. R. Acad. Sci. (Paris)*, 1908, **146**, 530.
26 P. Hanggi, P. Talkner and M. Borkovec, *Rev. Mod. Phys.*, 1990, **62**, 251.
27 O. K. Dudko, G. Hummer and A. Szabo, *Phys. Rev. Lett.*, 2006, **96**, 108101.
28 H.-J. Lin, H.-Y. Chen, Y.-J. Sheng and H.-K. Tsao, *Phys. Rev. Lett.*, 2007, **98**, 088304.
29 Y. Seol, D. L. Stein and K. Visscher, *Phys. Rev. Lett.*, 2009, **103**, 050601.
30 M. Arrayás, I. Kh. Kaufman, D. G. Luchinsky, P. V. E. McClintock and S. M. Soskin, *Phys. Rev. Lett.*, 2000, **84**, 2556.
31 J. W. Haus and K. W. Kehr, *Phys. Rep.*, 1987, **150**, 263.
32 S. Havlin and D. Ben-Avraham, *Adv. Phys.*, 2002, **51**, 187.
33 Z.-H. Hu, L.-W. Cheng and B. J. Berne, *J. Chem. Phys.*, 2010, **133**, 034105.
34 J. C. Crocker and D. G. Grier, *J. Colloid Interface Sci.*, 1996, **179**, 298.
35 P. N. Pusey, in *Liquids, freezing and glass transition*, ed. J. P. Hansen, D. Levesque and J. Zinn-Justin, North-Holland, Amsterdam, 1991, ch. 10.
36 B. P. Binks and T. Horozov, *Colloidal particles at liquid interfaces*, Cambridge University Press, Cambridge, UK, 2006.
37 L. P. Faucheux, G. Stolovitzky and A. Libchaber, *Phys. Rev. E: Stat. Phys., Plasmas, Fluids, Relat. Interdiscip. Top.*, 1995, **51**, 5239.
38 P. Reimann, C. Van den Broeck, H. Linke, P. Hanggi, M. Rubi and A. Perez-Madrid, *Phys. Rev. Lett.*, 2001, **87**, 010602.
39 S. H. Lee and D. Grier, *Phys. Rev. Lett.*, 2006, **96**, 190601.
40 P. T. Korda, M. B. Taylor and D. Grier, *Phys. Rev. Lett.*, 2002, **89**, 128301.
41 L. R. Huang, E. C. Cox, R. H. Austin and J. C. Sturm, *Science*, 2004, **304**, 987.
42 F. Reif, *Fundamentals of Statistical and Thermal Physics*, McGraw-Hill, Auckland, 1985.
43 M. Schmiedeberg, J. Roth and H. Stark, *Eur. Phys. J. E: Soft Matter Biol. Phys.*, 2007, **24**, 367.
44 X. Qiu, X. L. Wu, J. Z. Xue, D. J. Pine, D. A. Weitz and P. M. Chaikin, *Phys. Rev. Lett.*, 1990, **65**, 516.
45 P. Tong, X. Ye and B. J. Ackerson, *Phys. Rev. Lett.*, 1997, **79**, 2363.
46 Y. Peng, W. Chen, Th. M. Fischer, D. A. Weitz and P. Tong, *J. Fluid Mech.*, 2009, **618**, 243.
47 W. Chen and P. Tong, *EPL*, 2008, **84**, 28003.
48 N. D. Denkov, O. D. Velev, P. A. Kralchevsky, I. B. Ivanov, H. Yoshimura and K. Nagayama, *Nature*, 1993, **361**, 26.

